NANO · MICRO small
www.small-journal.com

Check for updates

Defect Nanostructure and its Impact on Magnetism of α-Cr_2O_3 Thin Films

Igor Veremchuk, Maciej Oskar Liedke,* Pavlo Makushko, Tobias Kosub, Natascha Hedrich, Oleksandr V. Pylypovskyi, Fabian Ganss, Maik Butterling, René Hübner, Eric Hirschmann, Ahmed G. Attallah, Andreas Wagner, Kai Wagner, Brendan Shields, Patrick Maletinsky, Jürgen Fassbender, and Denys Makarov**

Thin films of the magnetoelectric insulator α-Cr_2O_3 are technologically relevant for energy-efficient magnetic memory devices controlled by electric fields. In contrast to single crystals, the quality of thin Cr_2O_3 films is usually compromised by the presence of point defects and their agglomerations at grain boundaries, putting into question their application potential. Here, the impact of the defect nanostructure, including sparse small-volume defects and their complexes is studied on the magnetic properties of Cr_2O_3 thin films. By tuning the deposition temperature, the type, size, and relative concentration of defects is tailored, which is analyzed using the positron annihilation spectroscopy complemented with electron microscopy studies. The structural characterization is correlated with magnetotransport measurements and nitrogen-vacancy microscopy of antiferromagnetic domain patterns. Defects pin antiferromagnetic domain walls and stabilize complex multidomain states with a domain size in the sub-micrometer range. Despite their influence on the domain configuration, neither small open-volume defects nor grain boundaries in Cr_2O_3 thin films affect the Néel temperature in a broad range of deposition parameters. The results pave the way toward the realization of spin-orbitronic devices where magnetic domain patterns can be tailored based on defect nanostructures without affecting their operation temperature.

1. Introduction

Antiferromagnetic spintronics relies on the use of metallic and insulating antiferromagnets to realize energy-efficient and ultra-fast memory and logic devices.[1,2] Cr_2O_3 possesses a unique place among insulating antiferromagnets as this material was the first compound in which the linear magnetoelectric (ME) effect was theoretically predicted[3] and experimentally observed.[4] Even 60 years after its discovery, Cr_2O_3 remains the only uniaxial antiferromagnet revealing a strong ME effect at room temperature, justifying its immediate relevance for spintronic and spin-orbitronic applications.[5–10] Due to these favorable properties, electrically switchable ME random access memory (MERAM) was realized at room temperature using Cr_2O_3 single crystals in exchange bias with a ferromagnetic film.[8,11] The ME effect also exists in thin films of Cr_2O_3,[12–18] which led to the realization of technologically appealing ferromagnet-free MERAM.[9]

While Cr_2O_3 single crystals display textbook antiferromagnetic behavior, such as macroscopic domains and spin-flop transitions,[19] structural defects in Cr_2O_3 thin films impact their properties, including the band structure,[20,21] mechanical,[21,22] and magnetic[22–24] properties. Although the films are well [0001] textured, they are formed of crystallites with each crystallite possessing further structural defects such as dislocation lines,[9] vacancies,[25] and grain boundaries.[26] The presence of these defects has been linked to the appearance of an

I. Veremchuk, P. Makushko, T. Kosub, O. V. Pylypovskyi, F. Ganss, R. Hübner, J. Fassbender, D. Makarov
Helmholtz-Zentrum Dresden-Rossendorf e.V.
Institute of Ion Beam Physics and Materials Research
Bautzner Landstrasse 400, 01328 Dresden, Germany
E-mail: i.veremchuk@hzdr.de; d.makarov@hzdr.de

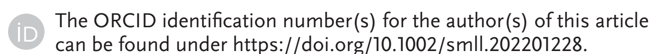
The ORCID identification number(s) for the author(s) of this article can be found under https://doi.org/10.1002/smll.202201228.

© 2022 The Authors. Small published by Wiley-VCH GmbH. This is an open access article under the terms of the Creative Commons Attribution License, which permits use, distribution and reproduction in any medium, provided the original work is properly cited.

DOI: 10.1002/smll.202201228

M. O. Liedke, M. Butterling, E. Hirschmann, A. G. Attallah, A. Wagner
Helmholtz-Zentrum Dresden-Rossendorf e.V.
Institute of Radiation Physics
Bautzner Landstrasse 400, 01328 Dresden, Germany
E-mail: m.liedke@hzdr.de

T. Kosub
Tensor Instruments
HZDR Innovation GmbH
01328 Dresden, Germany

N. Hedrich, K. Wagner, B. Shields, P. Maletinsky
Department of Physics
University of Basel
Klingelbergstrasse 82, Basel 4056, Switzerland

O. V. Pylypovskyi
Kyiv Academic University
Kyiv 03142, Ukraine

16136829, 2022, 17, Downloaded from https://onlinelibrary.wiley.com/doi/10.1002/smll.202201228 by Universitätsbibliothek Basel, Wiley Online Library on [03/09/2024]. See the Terms and Conditions (https://onlinelibrary.wiley.com/terms-and-conditions) on Wiley Online Library for rules of use; OA articles are governed by the applicable Creative Commons License

uncompensated magnetic moment[9] and even to a weakly ferromagnetic response of thin-film samples[25,22] and parasitic magnetism[27,28] as was reported recently. Furthermore, structural defects have a severe influence on the ME performance of Cr_2O_3-based antiferromagnetic MERAM (AF-MERAM) by enhancing the voltage needed for the operation of the memory cell.[9] This lack of understanding is linked to the challenges related to the quantification of defects and correlating them with integral and local magnetic responses of Cr_2O_3 thin films. The missing fundamental knowledge on the impact of defects on the magnetism of Cr_2O_3 thin films restricts the possibility of tailoring the spintronic performance of Cr_2O_3-based devices.

Here, we experimentally investigate the defect nanostructure of magnetron-sputtered 250-nm-thick Cr_2O_3 thin films prepared under different conditions on single crystals of Al_2O_3 (0001) and correlate it with the integral and local magnetic properties of the samples. We evaluate the type and relative concentration of defects. For this purpose, positron annihilation spectroscopy (PAS) was used as a unique probe for open-volume defects in thin films. The results obtained for thin-film samples are compared to single-crystal data. We find that single crystals are characterized by the formation of single-atom defects (monovacancies) in the sub-surface region. In thin films, we observe the formation of monovacancies, dislocations, and their loops, but also more complex defects, including vacancy clusters at grain boundaries. The type and quantity of all defects can be controlled by the sample fabrication procedure. The defect nanostructure strongly affects the magnitude of the electrical readout, which is measured of the Cr_2O_3 samples capped with a thin layer of Pt relying on the spin Hall effect. Furthermore, the presence of larger defects like grain boundaries has a strong influence on the pinning of magnetic domain walls in thin films. Independent of these findings, we show that the Néel temperature, which is one of the important technological metrics, is hardly affected by the formed defects in a broad range of deposition parameters. Our study has far-reaching consequences for the field of Cr_2O_3-based spin-orbitronic devices. Namely, our data suggest that the manipulation of the antiferromagnetic domain pattern in thin films of Cr_2O_3 can be done by adjusting the grain structure of the fully relaxed Cr_2O_3 thin film without any detrimental effect on its operation temperature.

2. Results and Discussion

The Cr_2O_3 thin films were grown at a nominal thickness of 250 nm using magnetron sputtering on Al_2O_3 (0001) substrates (**Figure 1**). By varying the deposition temperature from 500 to 900 °C, thin films of different structural quality were produced (**Table 1**). Due to the lattice mismatch between Cr_2O_3 and Al_2O_3, Cr_2O_3 initially grows strained. However, as the film grows, misfit dislocations are introduced, resulting in a buckled surface and the relaxation of individual grains. Still, the surface remains the thermodynamically stable (0001) facet. The boundary exhibits the important uncompensated surface magnetic monolayer boundary configuration when the material is in the antiferromagnetic state.[29,30]

With transmission electron microscopy (TEM), we confirmed that the films are phase-pure and possess the same corundum-type lattice as the Cr_2O_3 single crystal (Figure 1a,c and Figure S1, Supporting Information). Spectrum imaging based on energy-dispersive X-ray spectroscopy (EDXS) done in scanning TEM mode (Figure S2, Supporting Information) shows that the intermixing zones at each of the interfaces are almost negligible. In the region close to the interface between the film and the substrate, the thin-film sample accommodates misfit dislocations (Figure 1b,c). High-resolution TEM analysis (Figure 1c and Figure S3, Supporting Information) reveals that each of the regions of light contrast in Figure 1b along the interface corresponds to the core of an interface misfit dislocation. Based on the TEM data, the spacing between misfit dislocations

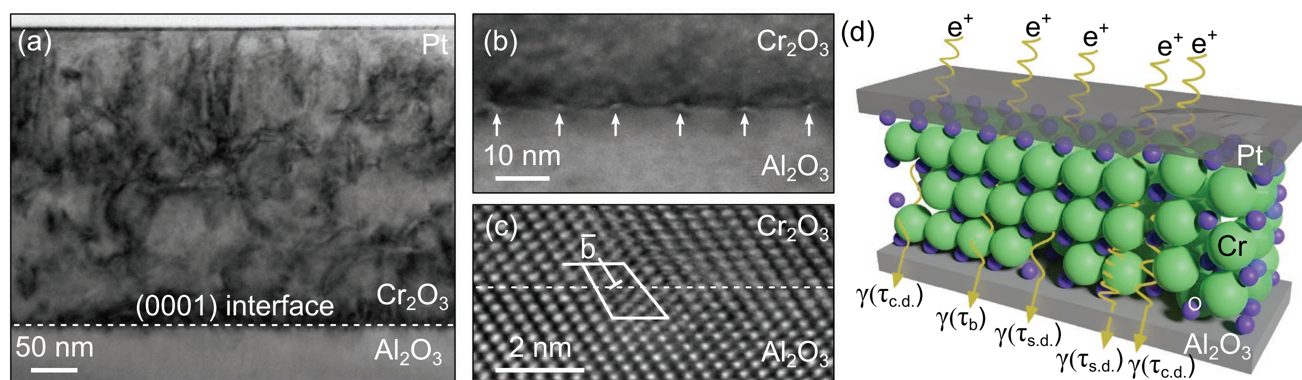

Figure 1. a) A cross-sectional overview TEM micrograph for the sample prepared at 700 °C and post-annealed at 750 °C in vacuum (sample #2, Table 1). The image was taken along the $[2\bar{1}\bar{1}0]$ zone axis and reveals the presence of internal defects, which cause contrast variations due to lattice bending. b) A bright-field TEM image shows the presence of misfit dislocations (light contrast indicated with arrows), which are periodically distributed along the interface to the substrate. c) High-resolution TEM image of the Cr_2O_3/Al_2O_3 interface region. The inset reveals the extra lattice plane as indicated by the white arrow. A Burgers circuit is drawn around one of the dislocations giving the projected magnitude of the Burgers vector. d) Schematics of a Cr_2O_3 thin film possessing different types of small-volume defects (monovacancies/dislocations) and complex defects. The interaction of positrons (e^+) with the sample leads to their annihilation at different defect sites. The detected photons (γ) carry information on the lifetime (τ) of the positrons, which is specific for the positron annihilation at simple defects (dislocations and monovacancies; $\tau_{s.d.}$), interstitials (τ_b), and complex defects (agglomeration of several monovacancies; $\tau_{c.d.}$).

© 2022 The Authors. Small published by Wiley-VCH GmbH

16136829, 2022, 17, Downloaded from https://onlinelibrary.wiley.com/doi/10.1002/smll.202201228 by Universitätsbibliothek Basel, Wiley Online Library on [03/09/2024]. See the Terms and Conditions (https://onlinelibrary.wiley.com/terms-and-conditions) on Wiley Online Library for rules of use; OA articles are governed by the applicable Creative Commons License

Table 1. Relevant parameters of the studied single crystal and thin films of Cr_2O_3.

#	T_{dep} [°C]	T_{an} [°C]	$\tau_{s.d.}$ [ps]	$\tau_{c.d.}$ [ps]	τ_r [ps]	τ_{av} [ps]	τ_b [ps]	$I_{s.d.}$ [%]	T_N [°C]
1	600	–	188	–	81–105	176		80–92	42(2)
2	700	750 (vacuum)	173–193	–	56–100	160	149	89–70	42(2)
3	800	–	183	358–410	–	184	–	86–98	41(3)
4	900	–	184	280–367	–	206	–	65–88	37(5)
5	500	700 (vacuum)	190	320–380	–	201	–	87–93	N/A
6	700	1000 (air)	141–166	255–380	–	212–260	–	60–83	40(2)

T_N stands for the Néel temperature, T_{dep} is the deposition temperature, and T_{an} is the annealing temperature applied to the sample after the deposition of the Cr_2O_3 thin films. $\tau_{s.d.}$ is the positron lifetime and the corresponding normalized intensity $I_{s.d.}$ of the Positron Annihilation Lifetime Spectroscopy (PALS) signal, which is related to the annihilation of positrons at monovacancies linked to dislocations (simple defects; s.d.). The positron lifetime $\tau_{c.d.}$ and the normalized PALS signal intensity $I_{c.d.}$ (=100% − $I_{s.d.}$) correspond to the annihilation of positrons inside complex defects (c.d.), for example, two or more monovacancies. The presence of the reduced bulk lifetime τ_r in the PALS spectra (and the corresponding PALS signal intensity I_r = 100% − $I_{s.d.}$) is a sign that the sample accommodates defects of only one type at a low concentration. τ_r was observed for samples #1 and #2. The average positron lifetime τ_{av} is the weighted average with respect to the contributions of the intensities related to $\tau_{s.d.}$ and $\tau_r/\tau_{c.d.}$ in the total PALS signal. The lifetime τ_b is the bulk lifetime, which corresponds to the annihilation of positrons at interstitial lattice positions (typical for high-quality single crystals). The measured here single-crystal reveals τ_b = 148(1) ps and T_N = 36(2) K. "N/A" stands for not accessible with the used measurement technique.

is determined to be 10.1(9) nm. We analyzed the region around the dislocation (Figure 1c) and evaluated a Burgers circuit around the core of one of the dislocations. The projected Burgers vector is parallel to the interface, and its amplitude is estimated to be $|\mathbf{b}| = \left|\frac{1}{2}\times[01\bar{1}0]\right| = \frac{\sqrt{3}}{2}a_{\text{film}}$ = 0.43 nm (for a_{film} = 0.496 nm, being the in-plane lattice parameter of the Cr_2O_3 film). The interface dislocation spacing can be estimated based on the relative ratio of the lattice parameters of Cr_2O_3 and Al_2O_3 ($\delta_f = [a_{\text{film}} - a_{\text{sub}}]/a_{\text{sub}} = 0.042$, where a_{sub} = 0.476 nm is the in-plane lattice parameter of the Al_2O_3 substrate) and the amplitude of the Burgers vector:[31–33] $d_{\text{md}} = |\mathbf{b}|/\delta_f = 10.2$ nm. A good agreement between the theoretical estimate and the experimentally measured value indicates that the lattice mismatch in 250-nm-thick Cr_2O_3 films prepared by magnetron sputtering is fully relaxed by interface dislocations.

Furthermore, TEM images clearly reveal the presence of internal defects (black bending contours in Figure 1a), which run through the entire sample. The structural nature of these defects can be attributed to grain boundaries. It is already established that the presence of grain boundaries in thin Cr_2O_3 films does have a major impact on the antiferromagnetic domain landscape for the samples prepared using electron beam evaporation.[9,26] To address the magnetic microstructure of the magnetron-sputtered Cr_2O_3 samples, we performed nitrogen-vacancy (NV) microscopy.[34] In this study, a diamond tip with a single spin defect is scanned over the surface of the sample and allowing us to image the local magnetic stray field pattern.[9,26,35] A marked difference in the antiferromagnetic domain pattern was observed between single crystals (Figure S4a, Supporting Information) and thin-film samples (Figure S4b, Supporting Information). The single crystal is primarily found to be in a single domain state over the entire sample area of 5×3 mm^2. Domain walls, if present in the sample, run straight and undisturbed over macroscopic distances (Figure S4a, Supporting Information).[5,10,11] In contrast, in thin films, the typical size of magnetic domains is in the range of several hundreds of nanometers (Figure S4b, Supporting Information). These domains encompass a few structural grains, and the domain walls prefer to run through the grain boundaries, which act as pinning sites for the domain walls. In this respect, the antiferromagnetic domain pattern in 250-nm-thick magnetron-sputtered films of Cr_2O_3 is similar to the one measured for electron beam evaporated Cr_2O_3 films with a thickness of 250 nm.[26]

One of the most technologically relevant parameters of magnetic devices is their operation temperature. In the case of antiferromagnetic materials, the upper limit for the operation temperature is given by the antiferromagnet–paramagnet transition temperature (the Néel temperature, T_N). We applied magnetotransport characterization to experimentally assess the Néel temperature of the samples (Table 1). For this study, the samples were capped with a 3-nm-thick Pt film. The transverse resistance of the Pt thin film is modified by the magnetism of the underlying Cr_2O_3 film as a result of the spin Hall magnetoresistance effect.[36,37] The Néel temperature can be extracted from the magnetotransport measurements by monitoring the temperature and magnetic field dependences of the transverse resistance (**Figure 2**). For this study, the magnetic state of the sample is prepared by cooling the samples down from 60 °C (paramagnetic state) to 15 °C (antiferromagnetic state) in the magnetic field of different strength and polarity oriented normal to the film plane. The magnetic-field-cooling process leads to a predominant selection[38] of one of the two possible antiferromagnetic domains in the sample, which is reflected in a transverse resistance readout (Figure 2a). After cooling the sample in the field of choice (here, ±7.5 kOe), the magnetic field is removed and the transverse resistance is recorded upon warming up in zero fields (Figure 2b). The transverse resistance readout is observed to decay with temperature and vanishes at the Néel temperature. Using this transport-based method, we establish that T_N of the studied Cr_2O_3 thin film samples is (40 ± 4) °C, similar to that of the single crystal (36 ± 2) °C; Table 1. This finding suggests that the magnetic order in Cr_2O_3 is very robust with respect to the different fabrication conditions and defect nanostructures. This result is encouraging, especially from the point of view of the design of antiferromagnetic spin-orbitronic memory devices relying on thin films of Cr_2O_3.

 © 2022 The Authors. Small published by Wiley-VCH GmbH

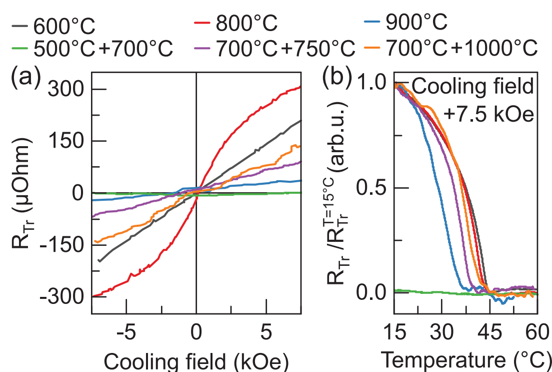

Figure 2. Magnetotransport characterization. a) The transverse resistance of the Pt electrode is measured as a function of the cooling field. The sample is cooled through the Néel temperature from 60 to 15 °C in the out-of-plane field between −7.5 and +7.5 kOe. b) The temperature evolution of the normalized transverse resistance of the Pt electrode upon zero-field warming process. For this experiment, the sample was initially field cooled in the field of +7.5 kOe. The Néel temperature is defined as a temperature, at which the signal vanishes.

We note that although close, the Néel temperature of our thin films is slightly higher than the bulk value. The Néel temperature is determined by the exchange coupling constants, which are sensitive to the interatomic distance between the magnetic ions and their respective bond-angle variations. The enhancement of T_N by the distortion of the lattice could be achieved through crystal structure modification. Theoretical calculations show that the Néel temperature of Cr_2O_3 can be increased by increasing the ratio between the out-of-plane (c) to the in-plane (a) lattice parameters. For instance, a 20% enhancement of T_N could be achieved by increasing the respective c/a ratio only by 5%.[23] We carried out X-ray diffraction (XRD) characterization of the thin film samples (Figure S5, Supporting Information) to understand their strain state. Analysis of the XRD data provides access to the out-of-plane (c) lattice parameter from the position of the 0006 Bragg reflection:

$$\frac{1}{d_{hkl}^2}=\frac{4}{3}\frac{h^2+hk+k^2}{a^2}+\frac{l^2}{c^2} \tag{1}$$

$$n\lambda=2d_{hkl}\sin\theta \tag{2}$$

where d is the interplane distance for a (hkl) plane, h k l are the Miller indices, θ is Bragg angle, a and c are the lattice parameters, n is the diffraction order. **Table 2** summarizes the determined c lattice parameters. To calculate the c/a ratio, we used the literature value of the in-plane lattice parameter (a) and the experimentally determined lattice parameter (c). The use of the literature value for the in-plane lattice parameter is justified by our experimental data (Figure 1b and Figure S3, Supporting Information), which shows fully relaxed thin films in the in-plane direction.

According to the analysis by Kota et al.,[23] the enhancement of the Néel temperature in Cr_2O_3 samples as a function of the c/a ratio reads:

$$\Delta T\left(\frac{c}{a}\right)\approx 251.7\left[\frac{c}{a}-\frac{c_0}{a_0}\right]^\circ\mathrm{C} \tag{3}$$

Table 2. Analysis of the XRD data (Figure S5, Supporting Information) allows accessing the c lattice parameter of our thin-film samples. We compare our data with the literature data on the relaxed a and c lattice parameters of single-crystalline Cr_2O_3.[39–41] As our experimental data based on the analysis of the spacing between misfit dislocations (Figure 1b and Figure S3, Supporting Information) indicates that the thin film samples are relaxed in the plane, we calculate the c/a ratio based on the a lattice parameter taken for single crystals and c lattice parameter determined from our XRD study. The column with ΔT indicates the estimated increase of the Néel temperature due to the presence of the homogeneous strain. The estimations are done based on the theory by Kota et al.[23]

	a [Å]	c [Å]	$\Delta c/c$ [%]	c/a	ΔT [%]
References [39–41]	4.959	13.593	0	2.741	–
600 °C	–	13.6499	0.42	2.752	2.89
800 °C	–	13.632	0.29	2.749	1.98
900 °C	–	13.643	0.37	2.751	2.54
500 °C + 700 °C	–	13.672	0.58	2.757	4.03
700 °C + 750 °C	–	13.626	0.24	2.748	1.76
700 °C + 1000 °C	–	13.622	0.21	2.747	1.47

where c_0 = 13.593 Å and a_0 = 4.959 Å are the values of the a and c lattice parameters of a single crystalline Cr_2O_3. Based on the data summarized in Table 2 and using the theory by Kota et al.,[23] we can estimate the expected increase of the Néel temperature due to the homogeneous strain in our samples. The estimated increase of the Néel temperature compared to the bulk value is about 2.5 °C. Considering that the literature data for the Néel temperature of single crystals is 37 °C,[3,39,42] a small homogeneous strain in our thin-film samples can explain the observed increase of the Néel temperature reported in Figure 2b.

In contrast to the robustness of the Néel temperature, the shape of the cooling field dependence of the transverse resistance is sensitive to the preparation conditions (Figure 2a). The samples prepared at growth temperatures higher than 600 °C do respond to the cooling magnetic field. It appears that growing the samples at 500 °C even with an additional post-annealing at 700 °C (sample #5, Table 1) is insufficient to realize an antiferromagnetic film responding to the field cooling procedure (green curve in Figure 2a). This finding is in line with the recent work by Vu et al.,[43] where it is reported that a good crystallinity is observed for Cr_2O_3 thin films grown at 700 °C (compare to the properties of thin films prepared at a lower temperature[44,45]). While the sample grown at 800 °C (sample #3, Table 1) reveals the strongest change of the transversal resistance (red curve in Figure 2a), the film prepared at 900 °C (sample #4, Table 1, blue curve in Figure 2a) shows the weakest measured transverse resistance change among all samples. This observation is in contrast to the expectation that higher growth temperature can result in further improvement of the structural quality of the Cr_2O_3 film suggesting its stronger magnetotransport response to the cooling field. We note that the magnitude of the transverse resistance is determined not only by the structural quality of the interior of the Cr_2O_3 film but also by the quality of the Cr_2O_3/Pt interface. Therefore, a more pronounced response to the field cooling of the samples prepared at 600 and 800 °C compared to the

 © 2022 The Authors. Small published by Wiley-VCH GmbH

16136829, 2022, 17, Downloaded from https://onlinelibrary.wiley.com/doi/10.1002/smll.202201228 by Universitätsbibliothek Basel, Wiley Online Library on [03/09/2024]. See the Terms and Conditions (https://onlinelibrary.wiley.com/terms-and-conditions) on Wiley Online Library for rules of use; OA articles are governed by the applicable Creative Commons License

900 °C one can be an indication of a more defective structure at this surface. Furthermore, we note that the samples, which were post-annealed yet prepared at 700 °C (samples #2 and #6, Table 1) reveal a weaker response to the cooling field compared to the sample grown at 600 °C (sample #1, Table 1) but without additional annealing. These observations hint at the impact of the defect nanostructure in the Cr_2O_3 thin films (interior and interfaces) caused by the different fabrication conditions on the magnitude of the transverse resistance. This is a key parameter determining the spintronic performance of the devices based on thin films of Cr_2O_3.

Considering that Cr_2O_3 is a material that has been around for more than 60 years, it is surprising that still so little is known about the defect nanostructure in technologically relevant thin films. TEM is very useful in answering questions regarding strain and large-scale lattice deformations but has limited use for determining the type of small open-volume defects. In this respect, experimental studies[46] of bulk chromia indicate that there are three different point defects, which strongly influence the electronic properties: Cr vacancies, Cr Frenkel defects (composed by an interstitial Cr atom and a Cr vacancy), and O vacancies. Theoretically, it was distinguished that the formation energy of the point defects follows the order: Cr Frenkel defect, Cr vacancy, and O vacancy.[20] Such defects can cause slight variations of the average valence of the Cr^{3+} ions and lead to marked changes in magnetism, which is exemplified by the high-temperature magnetic order[25,46] of CrO_2 or of CrN in comparison with Cr_2O_3. PAS offers the sensitivity exactly for this kind of sparse small-volume defects, which are impossible to characterize with other structural techniques.[47] The main idea of PAS is that positrons penetrate the solid and then annihilate with core and valence electrons of the material, thereby emitting two ≈511 keV gamma photons (Figure 1a). Due to the electron momentum, the change in this value is the result of the Doppler broadening of the annihilation line, which is characterized by the shape parameter (S) and the wing parameter (W). The depth sensitivity of the technique is determined by the change in the energy of incidence of positrons E_p, which leads to different depths of penetration of positrons.

The PAS data taken for the thin film samples prepared at different conditions (Table 1) is shown in Figure S6, Supporting Information (for the single crystal [Figure S6a, Supporting Information] and thin films [Figure S6b,c, Supporting Information]). The analysis of the S-parameter reveals a significantly enhanced trapping potential for higher-energy positrons at the Cr_2O_3/Al_2O_3 interface, corresponding to an enhanced defect concentration compared to the interior of the thin film. The positron trapping in the interior of thin films is likely due to vacancy-like defects or dislocations. For lower energy positrons, their large fraction annihilates at the surface and sub-surface defects. This behavior is in contrast to the one observed for the single crystal, where it is possible to identify a sub-surface region with a depth of about 65 nm, where a large concentration of monovacancy-like defects was detected due to polishing of the single-crystal surface.

For the analysis of the types of defects and their concentrations, we carried out sandwich Positron Annihilation Lifetime Spectroscopy (PALS) measurements. This study performed on the Cr_2O_3 single crystal revealed delocalized annihilation

Table 3. DFT-calculated positron lifetime for annihilation processes in Cr_2O_3. The positron lifetimes corresponding to the annihilation at Cr vacancies (V_{Cr}), oxygen vacancies (V_O), bi-vacancies of Cr-O ($V_{Cr}V_O$), and Cr-Cr (V_{2xCr}) are listed in the respectively indicated column of the table. The positron lifetime due to annihilation at interstitials (bulk annihilation, τ_b) is 151.7 ps. This annihilation process is typical for high-quality single crystals.

Defect type	V_{Cr}	V_O	$V_{Cr}V_O$	V_{2xCr}
Positron lifetime (ps)	197.4	153.7	214.0	205.2

with a positron lifetime of about $\tau_b \approx 148(1)$ ps. Since there is no literature data on the defect states in chromia, we have conducted calculations of positron lifetimes for the annihilation at interstitials and different defects relying on the atomic superposition (ATSUP) approach using two-component density functional theory (DFT) calculations (**Table 3** and Tables S1 and S2, Supporting Information). The calculated lifetime values are in agreement with the experimentally measured data (compare data summarized in Tables 1 and 2). Furthermore, it is insightful to note that the lifetime for defects in the chromia can be estimated rather accurately by scaling the Al_2O_3 positron data[48] (see also Figure S7, Supporting Information) to the difference in the unit cell volume for Cr_2O_3 and Al_2O_3 (12% larger for Cr_2O_3). For Al_2O_3, the positron lifetime of $\tau_{s.d.} \approx 165$ ps corresponds to a monovacancy, and $\tau_{c.d.} = 190–220$ ps is ascribed to a bi-vacancy.[49]

Similar to the case of Al_2O_3, the analysis of the PALS data taken for the Cr_2O_3 thin-film samples allows us to identify two characteristic positron lifetimes ($\tau_{s.d.}$ and $\tau_{c.d.}$), which are summarized for the entire sample series in Table 1 (see also Table S1, Supporting Information). The relaxation time $\tau_{s.d.}$ varies between 81 and 190 ps and is related to the annihilation of positrons in the interior of the film as well as at dislocations, likely mixed with Cr monovacancies (simple defects; s.d.). Both types of defects usually have a similar lifetime, although the lifetime for dislocations should be between the one for the interstitials (bulk annihilation, τ_b) and V_{Cr}.[50,51] Moreover, for the samples prepared at 600 and 700 °C (samples #1 and #2, respectively; Table 1), the positron lifetime is found to be even shorter than the lifetime related to the annihilation of positrons at interstitials, τ_b. This so-called reduced lifetime (τ_r) can be observed in materials with only one type of defect. In this case, positrons annihilate predominantly on point defects like dislocations/monovacancies. The observation of the reduced lifetime in these samples is a fingerprint of their high quality in terms of the presence of small-volume defects and their low concentration. In turn, having the relaxation time in the range of 200 to 400 ps corresponds to the positron annihilation at vacancy clusters (a complex defect composed of 2 up to ≈20 vacancies; $\tau_{c.d.}$). The analysis of the signal intensities ($I_{s.d.}$ and $I_{c.d.}$, Table 1) related to $\tau_{s.d.}$ and $\tau_{c.d.}$ suggests that most of the positrons (about 90%) annihilate at dislocations combined with monovacancies. These conclusions are in agreement with prior calculations,[20] indicating that Cr Frenkel defects composed of an interstitial Cr atom and a Cr vacancy are energetically more favorable than monovacancies. While complex defects are theoretically predicted to form at low temperatures, the formation of monovacancies and dislocations is facilitated at higher

© 2022 The Authors. Small published by Wiley-VCH GmbH
16136829, 2022, 17, Downloaded from https://onlinelibrary.wiley.com/doi/10.1002/smll.202201228 by Universitätsbibliothek Basel, Wiley Online Library on [03/09/2024]. See the Terms and Conditions (https://onlinelibrary.wiley.com/terms-and-conditions) on Wiley Online Library for rules of use; OA articles are governed by the applicable Creative Commons License

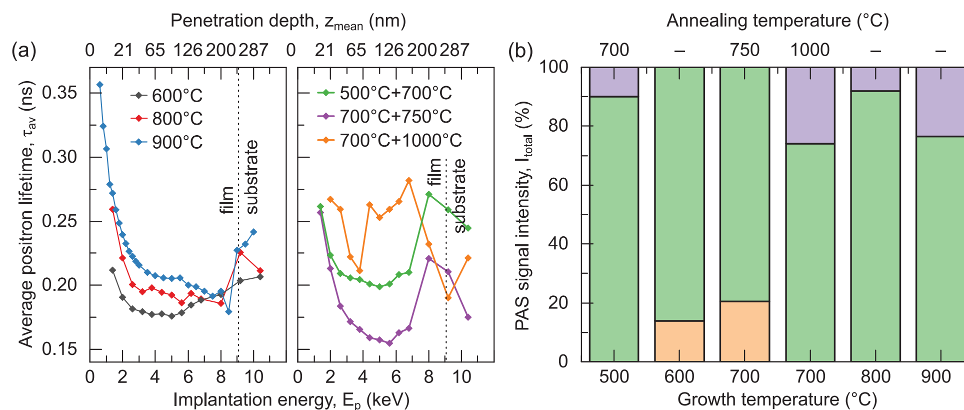

Figure 3. Positron annihilation spectroscopy study. a) Depth profiles of the average positron lifetime τ_{av} for samples prepared at different conditions (Table 1). b) Qualitative assessment of the sample quality in terms of small-volume defects. The plot of the contributions to the total PAS signal intensity: intensity related to the positron relaxation time of 150 ps < τ < 200 ps is marked in green (relaxation on simple defects like dislocations combined with monovacancies); intensity related to the positron relaxation time of τ > 200 ps is marked in purple (relaxation on complex defects consisting of several vacancies); intensity related to the positron lifetime with τ < 150 ps is marked in orange (relaxation typical for the films with only one defect type; here, dislocations/monovacancies).

temperatures. We note that the contribution of complex vacancy clusters to the overall signal (the $I_{c.d.}$ = 100% – $I_{s.d.}$ part of the signal intensity, corresponding to the $\tau_{c.d.}$; Table 1) is found to be rather small, beside the sub-surface region.

It is convenient to assess the quality of the samples by analyzing the average positron lifetime τ_{av} (**Figure 3**a), which is weighted with respect to the contributions of the intensities related to $\tau_{s.d.}$, and $\tau_{c.d.}$ (or τ_r for the samples #1 and #2) in the total PALS signal (Table 1). The analysis of the combined PAS data (Figure 3 and Figures S6 and S8, Supporting Information) indicates the following trend: the increase of the growth temperature i) reduces the overall density of defects in Cr_2O_3 films yet ii) favors the formation of vacancy agglomerations, and iii) results in the modification of the top surface of Cr_2O_3 thin films. The samples grown at higher temperatures show an increase in τ_{av} in the region of the top surface (Figure 3a, region of low implantation energy), suggesting an increase in the complexity of defects and their concentration in the sub-surface region. This is especially pronounced for the Cr_2O_3 film grown at 900 °C (sample #4, Table 1, blue curve in Figure 3a). This finding is in line with the magnetotransport data (Figure 2a blue curve), indicating that the change of the transverse resistance with the cooling field of the sample prepared at 900 °C is substantially reduced compared to the samples prepared at lower temperatures. The quality of the interface between Pt and Cr_2O_3 affects the spin-orbitronic parameters, like spin mixing conductivity, which are responsible for the magnitude of the transverse resistance due to the spin Hall effect.[52–54]

Additional post-annealing changes the spatial profile of the defects across the sample thickness and especially affects the defect chemistry at the bottom Cr_2O_3/Al_2O_3 interface. Post-annealing in vacuum (growth temperature of 700 °C and post-annealing at 750 °C; sample #2, Table 1) allows us to obtain the lowest overall concentration of small-volume defects (purple curve in Figure 3a). Still, the sample possesses a substantial increase in the concentration of small-volume defects at the top and bottom interfaces compared to the interior of the film. The reduction of the quality of the Pt/Cr_2O_3 interface does not allow to achieve a large change of the transverse resistance for this sample independent of its good structural quality in the interior. Post-annealing in the air (growth temperature of 700 °C and post-annealing at 1000 °C; sample #6, Table 1) leads to the largest overall open volume, likely modifying grain boundaries.

Following this analysis, we plot a semi-quantitative map representing the sample quality in terms of the small-volume defects (Figure 3b). We determine that for all samples, the prevalent defect type is a dislocation, likely coupled to a monovacancy (Figure 3b, green-shaded region). The samples grown at temperatures lower than 600 °C and higher than 700 °C also contain complex defects with large vacancy clusters with up to six missing atoms according to the DFT calculation (Figure 3b, violet-shaded region and Figure S8 and Table S2, Supporting Information). The highest structural quality is obtained for the samples grown at 600 °C (sample #1; Table 1) and 700 °C post-annealed at 750 °C in a vacuum (sample #2; Table 1). Those samples contain no complex open-volume defects (the positron relaxation time is found to be smaller than 200 ps; Table 1). Furthermore, they show a reduced positron lifetime (τ_r), which indicates that the thin films are characterized by the formation of only point defects like dislocations/monovacancies, and their concentration is low (Figure 3b, orange-shaded region and Figure S8, Supporting Information).

3. Conclusion

In summary, we analyzed the defect nanostructure in magnetron-sputtered 250-nm-thick films and addressed its impact on the integral and local magnetic properties. Our analysis reveals that the Cr_2O_3 thin films are characterized by the presence of complex defects at grain boundaries, formed by a group of monovacancies, coexisting with monovacancies and dislocations. The concentration of complex defects can be controlled by the sample fabrication conditions, including the deposition temperature as well as the post-annealing in vacuum or air. We determined that the defects and hence the sample fabrication conditions have very little influence on the Néel temperature.

 © 2022 The Authors. Small published by Wiley-VCH GmbH

16136829, 2022, 17, Downloaded from https://onlinelibrary.wiley.com/doi/10.1002/smll.202201228 by Universitätsbibliothek Basel, Wiley Online Library on [03/09/2024]. See the Terms and Conditions (https://onlinelibrary.wiley.com/terms-and-conditions) on Wiley Online Library for rules of use; OA articles are governed by the applicable Creative Commons License

The magnetotransport characterization indicates that the measured transverse resistance in response to the magnetic cooling field is very different for the samples prepared under different conditions. Based on the surface sensitivity of the magnetotransport characterization in oxide antiferromagnets via spin Hall effect,[55] we attribute the change of the small-volume defects at the top region of the thin film samples as the reason for the change of their spin-orbitronic performance.

While single crystals allow for the formation of millimeter-large domains, in thin films, the domains have sub-µm size due to the pinning of antiferromagnetic domain walls at grain boundaries. The physical mechanism of the pinning of antiferromagnetic domain walls in thin films of Cr_2O_3 is still to be addressed theoretically and experimentally. A fundamental understanding of the domain walls pinning can potentially enable further ideas of the recording medial based on Cr_2O_3. With our present study, we demonstrate that the manipulation of the magnetic microstructure can be done independently of the modification of the Néel temperature. This is an important technological aspect, which is crucial for the further application of fully relaxed Cr_2O_3 thin films for prospective spin-orbitronic devices.

4. Experimental Section

Cr_2O_3 Samples: The Cr_2O_3 thin films were grown by magnetron sputter deposition (base pressure: 10^{-7} mbar; Ar sputter pressure: 10^{-3} mbar; deposition rate: 0.4 Å s^{-1}) of a pure Cr_2O_3 target material (Robeko GmbH & Co. KG). To initiate the crystallization of the Cr_2O_3, single-crystalline Al_2O_3 (0001) substrates (Crystec GmbH) were heated to 850 °C before the deposition. The Cr_2O_3 thin films were deposited at different temperatures ranging from 500 to 900 °C. Additionally, after deposition, some samples were further annealed at temperatures higher than the deposition temperature in vacuum or air (Table 1). A 1-mm-thick Cr_2O_3 single crystal (MaTecK) with (0001) surface orientation was used as a reference sample. For the magnetotransport characterization, the Cr_2O_3 samples were capped with a 3-nm-thick Pt top layer deposited in situ using magnetron sputtering at a temperature below 100 °C at the rate of 1 Å s^{-1} (Ar sputter pressure: 10^{-3} mbar).

The chosen range of deposition temperatures is typical for the research on Cr_2O_3 thin films. For instance, thin films grown on (0001) Al_2O_3 in the temperature range of 300–500 °C show many individual columnar grains in the *c*-direction with a mosaic spreading. The interface between the thin film and substrate is partially coherent and characterized by periodic misfit dislocations.[44,45] Good crystallinity of Cr_2O_3 thin films is observed when they are grown at 700 °C.[43] Furthermore, post-annealing of the room temperature grown Cr_2O_3 thin films shows an increase in the size of individual grains.[56]

Transmission Electron Microscopy Studies: TEM analysis was conducted on thin cross-sections of specimens. Classical TEM cross-sections glued together in face-to-face geometry using G2 epoxy glue (Gatan) were prepared by sawing (Wire Saw WS 22, IBS GmbH), grinding (MetaServ 250, Bühler), polishing (Minimet 1000, Bühler), dimpling (Dimple Grinder 656, Gatan), and final Ar ion milling (Precision Ion Polishing System PIPS 691, Gatan). Cross-sectional bright-field TEM imaging, selected-area electron diffraction, and high-resolution TEM imaging were performed using an image-C_s-corrected Titan 80–300 microscope (FEI) operated at an accelerating voltage of 300 kV. High-angle annular dark-field scanning transmission electron microscopy (HAADF-STEM) imaging and spectrum imaging analysis based on EDXS were performed with a Talos F200X microscope (FEI) operated at 200 kV. Prior to (S)TEM analysis, the specimen mounted on a high-visibility low-background holder was treated for 8 s with a Model 1020 Plasma Cleaner (Fischione) to remove potential contamination.

X-Ray Diffraction: Phase identification was performed by Rigaku SmartLab 3kW with a parallel beam of Cu $K_{\alpha 1}$ radiation, λ = 1.54056 Å, and 2θ range 30°–50° (using a Ge [220] two-bounce monochromator). The reflection positions obtained by the profile deconvolution were corrected using the Al_2O_3 substrate. Lattice parameters refinement was performed with WinCSD.[57] The XRD data shown in Figure S5, Supporting Information, revealed the presence of only 0006 Bragg reflection from the Cr_2O_3 thin films as well as from the Al_2O_3 substrate. This finding confirmed the high quality of the thin films, which were essentially a single crystal in perfect registry with the substrate. As can be seen from the XRD data, the position of the thin film's reflections was slightly different for all thin films. This indicated that the lattice parameters of different films may have changed due to epitaxial strain, thermal strain, or intrinsic residual strain. The *c* lattice parameter for respective thin films was calculated (Table 2). The reflection of the thin films was rather broad. The main source of the peak broadening was caused by the size of the crystal domain.

Magnetotransport Measurements: The transverse resistance of the Pt thin film electrode was measured using the Zero-Offset Hall preset of a Tensormeter measurement device (HZDR Innovation GmbH, Germany). This mode provides the absolute transverse resistance without any offset due to undetermined sample geometry.[9,17]

Positron Annihilation Spectroscopy: Defect concentration depth profiling of 250-nm-thick Cr_2O_3 films and a Cr_2O_3 single-crystal was carried out with the monoenergetic positron beam at the large-scale facility ELBE of the Helmholtz–Zentrum Dresden–Rossendorf.[58,59] The setup allowed for tuning the positron energy E_p from 30 eV to 36 keV. The energy resolution of the Ge detector at 511 keV was 1.09(1) keV, resulting in a high sensitivity to changes in material properties from surface to depth. About 5×10^5 events per spectrum were accumulated. For analysis of the experimental data, the positron stopping profiles were approximated by a Makhovian distribution, and the mean positron penetration depth was $z_{mean} = A \rho^{-1} E_p^{\,n}$, where E_p is the positron energy, ρ is the material density, and the parameters *A* and *n* are material-related constants.[60] The $S(E_p)$ dependence was fitted with the VEPFIT code[60] to calculate the effective diffusion lengths, *L*+, in the system as well as the characteristic *S*-parameters. Standard model 5 of VEPFIT was used to fit the data, where a rectangular distribution of defects and a layered structure were assumed. Three distinct regions were considered for the thin film, two of them with thicknesses of 250 and 5 nm for a film-bulk and a film interface, respectively. The third region was the Al_2O_3 substrate. Only one region can be observed for the single crystal with a thickness of ≈65 nm (Figure S6a, Supporting Information). The fitting zone for the VEPFIT calculation was divided into 48 depth intervals starting with 0.1 nm and with an increment factor of 1.3.

Representative PAS data for the thin film samples prepared at different conditions (Table 1) are shown in Figure S6b,c, Supporting Information, and compared to a single crystal (Figure S6a, Supporting Information). The maximum positron implantation depth was about $2 \times z_{mean}$ (calculated values for z_{mean} are indicated in Figure S6, Supporting Information, as the bottom *x*-axis). The $S(E_p)$ curve indicated an increased open volume at the implantation energy of $E_p \approx 9$ keV, which corresponded to $z_{mean} \approx 242$ nm, thus very close to the expected interface position (Figure S6b,c, Supporting Information). Such an increase represented the positron trapping at defects localized in this particular area.[9] The positron energy of $E_p \approx 5$ keV corresponded to the depth of $z_{mean} \approx 94$ nm at which a major portion of positrons annihilate in the Cr_2O_3 film only (Figure S6b,c, Supporting Information). For lower energies, a large fraction of positrons additionally annihilate at the surface and sub-surface defects, which was reflected as an increased *S*-parameter. In the case of a single crystal, the interface region was absent. Instead, the dependence of the *S*-parameter ($1 < E_p < 3.5$ keV) had a plateau in the sub-surface region representing a larger concentration of vacancy-like defects.

The best fit values for the *S*-parameters of representative sample #2 in Table 1 (grown at 700 °C and post-annealed at 750 °C) were

© 2022 The Authors. Small published by Wiley-VCH GmbH

16136829, 2022, 17, Downloaded from https://onlinelibrary.wiley.com/doi/10.1002/smll.202201228 by Universitätsbibliothek Basel, Wiley Online Library on [03/09/2024]. See the Terms and Conditions (https://onlinelibrary.wiley.com/terms-and-conditions) on Wiley Online Library for rules of use; OA articles are governed by the applicable Creative Commons License

16136829, 2022, 17, Downloaded from https://onlinelibrary.wiley.com/doi/10.1002/smll.202201228 by Universitätsbibliothek Basel, Wiley Online Library on [03/09/2024]. See the Terms and Conditions (https://onlinelibrary.wiley.com/terms-and-conditions) on Wiley Online Library for rules of use; OA articles are governed by the applicable Creative Commons License

summarized in Table S1, Supporting Information. The effective positron diffusion lengths, *L*+, for the interface and substrate regimes were fixed in the calculation, whereas for the film-bulk region, *L*+ was left a free parameter, yielding the best fit for values of about 1 nm (interface region) and 45 nm (in the Al_2O_3 substrate). The diffusion length for the substrate was evaluated from the additional Doppler broadening variable energy positron annihilation spectroscopy (DB-VEPAS) measurement on a single-crystalline Al_2O_3 substrate (Figure S7, Supporting Information) and agreed with previous reports.[61]

The calculated *S*-parameters of the layers revealed a significantly enhanced trapping potential in the film-interface region corresponding to an enhanced defect concentration at the Cr_2O_3/Al_2O_3 interface compared to the bulk of the Cr_2O_3 film. The positron trapping in the film was likely due to vacancy-like defects or dislocations.

DB-VEPAS $S(E_p, z_{mean})$ dependencies for samples annealed during the deposition contained similar characteristic regions, that is, sub-surface, film-bulk, and interface. In the case of post-annealed films, the sub-surface and film-bulk regions were still clearly distinguishable. However, besides the sample grown at 700 °C and post-annealed at 750 °C in vacuum (sample #2; Table 1), the interface did not possess a clear maximum, which was an indicator of dislocation clusters. Interestingly, all the curves were very similar to the results obtained of a single crystal (Figure S6a, Supporting Information). Considering only samples deposited at temperatures above 600 °C, the *S*-parameter decreased as a function of temperature, indicating the reduction of the defect size and/or concentration.

Calculation of Defect Positron Lifetimes: Theoretical calculations of positron lifetimes for the bulk and defect states relying on the ATSUP approach using two-component DFT calculations were conducted.[62] For the electron–positron correlation, the generalized gradient approximation (GGA) scheme was used.[63] The atomic relaxations around defect sites were not considered.

Positron Annihilation Lifetime Spectroscopy: Variable energy positron annihilation lifetime spectroscopy (VEPALS) measurements were conducted at the monoenergetic positron source (MePS) beamline at Helmholtz–Zentrum Dresden–Rossendorf.[58] A digital lifetime $CrBr_3$ scintillator detector coupled to a SPDevices ADQ14DC-2X digitizer with 14-bit vertical resolution and 2 GS/s horizontal resolution was utilized,[64] and with a time resolution function down to about 0.250 ns. All spectra contained at least 10^7 counts. Typical lifetime spectrum $N(t)$ is described by $N(t) = \Sigma\ (1/\tau_i)\ I_i\ \exp(-t/\tau_i)$, where τ_i and I_i are the positron lifetime and intensity of the *i*th component, respectively ($\Sigma I_i = 1$). Each spectrum was deconvoluted using the package PALSfit[65] into two distinct lifetime components, which directly evidence the localized annihilation processes at two different defect types (monovacancies/dislocations [τ_1] and vacancy agglomerations [τ_2]). In addition, the presence of the bulk annihilation time, τ_b, was monitored corresponding to the delocalized annihilation on interstitials. For the samples grown at 600 and 700 °C (samples #1 and #2, respectively; Table 1), the positron lifetime is found to be shorter than the bulk lifetime, τ_b. This is reduced lifetime (τ_r). In this case, the localized annihilation can happen on only one defect type like monovacancies/dislocations. To avoid confusion in the discussion, in the main text of the manuscript, the positron lifetime τ_1 was referred to, which was related to the annihilation of simple defects, as $\tau_{s.d.}$. Furthermore, the positron lifetime τ_2 was referred, which was related to the annihilation of complex defects (two and more vacancies), as $\tau_{c.d.}$. For samples #1 and #2 (Table 1), there were no annihilation processes on complex defects. Instead, reduced lifetime, τ_r, was observed. In the fitting procedure discussed above, the reduced lifetime corresponded to the signal related to the fit with the component τ_1 possessing intensity I_1 (Figure S8, Supporting Information). Therefore, the annihilation on simple defects for these two samples was fitted with the component τ_2 possessing intensity I_2 (Figure S8, Supporting Information).

No contribution of grain boundaries to the positron lifetime was found for the samples deposited at 600 °C (sample #1, Table 1) and 700 °C and post-annealed at 750 °C in vacuum (sample #2, Table 1). The corresponding relative intensities reflected variations of the defects density as long as the size of the compared defects was in a similar range. In general, positron lifetime was linked to the defects size, that is, the larger the open volume, the lower the probability and the longer it takes for positrons to be annihilated with electrons.[66]

Increasing the deposition temperature to 800 °C (sample #3, Table 1) and 900 °C (sample #4, Table 1) does not remove the excess of vacancy-like defects. On the contrary, the reduced positron lifetime was not detectable anymore and positrons were trapped by monovacancies, likely as complexes with dislocations (note that the lifetime was slightly lower than calculated for a monovacancy), and larger vacancy clusters (at least six vacancies in a complex according to Table S2, Supporting Information) associated with grain boundaries. Since the *S*-parameter was smaller for the sample prepared at 800 °C compared to the one grown at 600 °C, the overall defect concentration must be smaller too. However, the increase of the average positron lifetime τ_{av} indicated that the net defect size had increased (Figure 3a). This was only possible due to the counteracting increase of the size and concentration of grain boundaries, especially in the sub-surface region.

For the samples prepared at low temperatures of 500 °C (even with post-annealing to 700 °C) or 900 °C, the impact of the grain boundaries became pronounced. Similarly, the increase of the open volume at the film-interface region was clearly visible in the data taken for the sample prepared at 700 °C and subsequently post-annealed in air at 1000 °C (Figure S8k, Supporting Information, sample #6 in Table 1). Comparing the intensities of the signals corresponding to τ_1 (indicated as $\tau_{s.d.}$ in Table 1) and τ_2 (indicated as $\tau_{c.d.}$ in Table 1), it can be seen that in this sample, the size of larger vacancy complexes decreased but their concentration dropped, suggesting smaller but more densely distributed grain boundary voids.

These results suggested that the structural properties of magnetron-sputtered chromia thin films were improved when the deposition temperature is kept within a window of 600–800 °C.

Nitrogen-Vacancy Scanning Magnetometry: NV magnetometry used an electronic spin-triplet ground state of an atomic NV defect in a diamond to measure stray fields.[67] A small bias field (below 60 Oe) was applied along the NV axis (54° from the normal of the sample) to split the states NV ms = $|\pm 1\rangle$. The magnetic stray field was proportional to the Zeeman splitting ms = $|\pm 1\rangle$ states, which made it possible to achieve a quantitative nanoscale image. To obtain images, one NV center was located on the tip of a fully diamond scanning probe[68] to provide scanning magnetometry with a spatial resolution of ≈50 nm. The image was performed using feedback to capture one of the NV resonances,[69] thus extracting the local field of scattered fluxes. The scattered field map was taken at room temperature using a special confocal scanning device.[70]

Supporting Information

Supporting Information is available from the Wiley Online Library or from the author.

Acknowledgements

I.V. and M.O.L. contributed equally to this work. The authors thank Rainer Kaltofen, Dr. Ingolf Mönch, and Conrad Schubert (all HZDR) for their support with the sputter deposition of the Cr_2O_3 thin films. The authors thank Romy Aniol and Dr. Hans-Jürgen Engelmann (both HZDR) for TEM specimen preparation. The authors thank Prof. Olav Hellwig (HZDR and TU Chemnitz) for providing access to the XRD facilities. Support by the Ion Beam Center and ELBE large-scale facilities at the HZDR is gratefully acknowledged. This work was partially supported by the Impulse- und Networking fund of the Helmholtz Association (FKZ VH-VI-442 Memriox), and the Helmholtz Energy Materials Characterization Platform (03ET7015). This work was financed in part via the German Research Foundation (DFG) Grant Nos. MA5144/22-1 and MA5144/24-1 and Helmholtz Association of German Research Centres

 © 2022 The Authors. Small published by Wiley-VCH GmbH

in the frame of the Helmholtz Innovation Lab "FlexiSens." Furthermore, the funding of TEM Talos by the German Federal Ministry of Education and Research (BMBF), Grant No. 03SF0451, in the framework of HEMCP is acknowledged.

Open access funding enabled and organized by Projekt DEAL.

Conflict of Interest

The authors declare no conflict of interest.

Data Availability Statement

The data that support the findings of this study are available from the corresponding author upon reasonable request.

Keywords

antiferromagnet, antiferromagnetic domains, Cr_2O_3 thin films, dislocations, magnetotransport, vacancy cluster

Received: February 24, 2022
Published online: March 28, 2022

[1] V. Baltz, A. Manchon, M. Tsoi, T. Moriyama, T. Ono, Y. Tserkovnyak, *Rev. Mod. Phys.* **2018**, *90*, 015005.
[2] T. Jungwirth, X. Marti, P. Wadley, J. Wunderlich, *Nature Nanotechnol.* **2016**, *11*, 231.
[3] I. E. Dzyaloshinskii, *J. Exp. Theor. Phys.* **1959**, *37*, 881.
[4] D. N. Astrov, *J. Exp. Theor. Phys.* **1960**, *38*, 984.
[5] M. Fiebig, *J. Phys. D* **2005**, *38*, R123.
[6] W. Eerenstein, N. D. Mathur, J. F. Scott, *Nature* **2006**, *442*, 759.
[7] P. Borisov, A. Hochstrat, X. Chen, W. Kleemann, C. Binek, *Phys. Rev. Lett.* **2005**, *94*, 117203.
[8] X. He, Y. Wang, N. Wu, A. N. Caruso, E. Vescovo, K. D. Belashchenko, P. A. Dowben, C. Binek, *Nat. Mater.* **2010**, *9*, 579.
[9] T. Kosub, M. Kopte, R. Hühne, P. Appel, B. Shields, P. Maletinsky, R. Hübner, M. O. Liedke, J. Fassbender, O. G. Schmidt, D. Makarov, *Nat. Commun.* **2017**, *8*, 13985.
[10] N. Hedrich, K. Wagner, O. V. Pylypovskyi, B. J. Shields, T. Kosub, D. D. Sheka, D. Makarov, P. Maletinsky, *Nat. Phys.* **2021**, *17*, 574.
[11] N. Wu, X. He, A. L. Wysocki, U. Lanke, T. Komesu, K. D. Belashchenko, C. Binek, P. A. Dowben, *Phys. Rev. Lett.* **2011**, *106*, 087202.
[12] N. Iwata, T. Kuroda, H. Yamamoto, *Jpn. J. Appl. Phys.* **2012**, *51*, 11PG12.
[13] T. Ashida, M. Oida, N. Shimomura, T. Nozaki, T. Shibata, M. Sahashi, *Appl. Phys. Lett.* **2014**, *104*, 152409.
[14] T. Ashida, M. Oida, N. Shimomura, T. Nozaki, T. Shibata, M. Sahashi, *Appl. Phys. Lett.* **2015**, *106*, 132407.
[15] K. Toyoki, Y. Shiratsuchi, A. Kobane, C. Mitsumata, Y. Kotani, T. Nakamura, R. Nakatani, *Appl. Phys. Lett.* **2015**, *106*, 162404.
[16] K. Toyoki, Y. Shiratsuchi, A. Kobane, S. Harimoto, S. Onoue, H. Nomura, R. Nakatani, *J. Appl. Phys.* **2015**, *117*, 17D902.
[17] T. Kosub, M. Kopte, F. Radu, O. G. Schmidt, D. Makarov, *Phys. Rev. Lett.* **2015**, *115*, 097201.
[18] J.-L. Wang, W. Echtenkamp, A. Mahmood, C. Binek, *J. Magn. Magn. Mater.* **2019**, *486*, 165262.
[19] M. Fiebig, D. Fröhlich, H.-J. Thiele, *Phys. Rev. B* **1996**, *54*, R12681.
[20] F. Lebreau, M. M. Islam, B. Diawara, P. Marcus, *J. Phys. Chem. C* **2014**, *118*, 18133.
[21] Z. Mi, L. Chen, C. Shi, Y. Ma, D. Wang, X. Li, H. Liu, L. Qiao, *Comput. Mater. Sci.* **2018**, *144*, 64.
[22] S. Punugupati, J. Narayan, F. Hunte, *Appl. Phys. Lett.* **2014**, *105*, 132401.
[23] Y. Kota, H. Imamura, M. Sasaki, *Appl. Phys. Express* **2013**, *6*, 113007.
[24] Y. Kota, H. Imamura, M. Sasaki, *J. Appl. Phys.* **2014**, *115*, 17D719.
[25] S. Punugupatia, J. Narayan, F. Hunte, *J. Appl. Phys.* **2015**, *117*, 193907.
[26] P. Appel, B. J. Shields, T. Kosub, N. Hedrich, R. Hübner, J. Faßbender, D. Makarov, P. Maletinsky, *Nano Lett.* **2019**, *19*, 1682.
[27] S. Ye, Y. Shiokawa, S. P. Pati, M. Sahashi, *ACS Appl. Mater. Interfaces* **2020**, *12*, 29971.
[28] S. Ye, Y. Shiokawa, S. P. Pati, M. Sahashi, *Phys. Status Solidi. Rapid Res. Lett.* **2019**, *13*, 1900135.
[29] K. D. Belashchenko, *Phys. Rev. Lett.* **2010**, *105*, 147204.
[30] F. Rohr, M. Bäumer, H.-J. Freund, J. A. Mejias, V. Staemmler, S. Müller, L. Hammer, K. Heinz, *Surf. Sci.* **1997**, *372*, L291.
[31] G. Gutekunst, J. Mayer, M. Ruhle, *Phil. Mag. A* **1997**, *75*, 1329.
[32] G. Gutekunst, J. Mayer, M. Ruhle, *Phil. Mag. A* **1997**, *75*, 1357.
[33] V. Vitek, G. Gutekunst, J. Mayer, M. Ruhle, *Phil. Mag. A* **1995**, *71*, 1219.
[34] J. Kölbl, M. Kasperczyk, B. Bürgler, A. Barfuss, P. Maletinsky, *New J. Phys.* **2019**, *21*, 113039.
[35] M. S. Wörnle, P. Welter, M. Giraldo, T. Lottermoser, M. Fiebig, P. Gambardella, C. L. Degen, *Phys. Rev. B* **2021**, *103*, 094426.
[36] R. Schlitz, T. Kosub, A. Thomas, S. Fabretti, K. Nielsch, D. Makarov, S. T. B. Goennenwein, *Appl. Phys. Lett.* **2018**, *112*, 132401.
[37] P. Muduli, R. Schlitz, T. Kosub, R. Hübner, A. Erbe, D. Makarov, S. T. B. Goennenwein, *Appl. Phys. Lett. Mater.* **2021**, *9*, 021122.
[38] K. Siratori, K. Kohn, E. Kita, *Acta Phys. Pol. A* **1992**, *81*, 431.
[39] S. Greenwald, *Nature* **1956**, *177*, 286.
[40] J. Graham, *J. Phys. Chem. Solids* **1960**, *17*, 18.
[41] M. Baster, F. Bourée, A. Kowalska, Z. Latacz, *J. Alloy Comp.* **2000**, *296*, 1.
[42] T. R. McGuire, E. J. Scott, F. H. Grannis, *Phys. Rev.* **1956**, *102*, 1000.
[43] N. M. Vu, X. Luo, S. Novakov, W. Jin, J. Nordlander, P. B. Meisenheimer, M. Trassin, L. Zhao, J. T. Heron, *Sci. Rep.* **2020**, *10*, 14721.
[44] Y. Gao, H. Leiste, M. Stüber, S. Ulrich, *J. Cryst. Growth* **2017**, *457*, 158.
[45] C. Sun, Z. Song, A. Rath, M. Street, W. Echtenkamp, J. Feng, C. Binek, D. Morgan, P. Voyles, *Adv. Mater. Interfaces* **2017**, *4*, 1700172.
[46] a) A. Holt, P. Kofstad, *Solid State Ionics* **1994**, *69*, 127; b) A. Holt, P. Kofstad, *Solid State Ionics* **1994**, *69*, 137.
[47] M. Khalid, M. Ziese, A. Setzer, P. Esquinazi, M. Lorenz, H. Hochmuth, M. Grundmann, D. Spemann, T. Butz, G. Brauer, W. Anwand, G. Fischer, W. A. Adeagbo, W. Hergert, A. Ernst, *Phys. Rev. B* **2009**, *80*, 035331.
[48] A. Uedono, K. Ikeuchi, K. Yamabe, T. Ohdaira, M. Muramatsu, R. Suzuki, A. S. Hamid, T. Chikyow, K. Torii, K. Yamada, *J. Appl. Phys.* **2005**, *98*, 023506.
[49] J. Xu, B. Somieski, L. D. Hulett, B. A. Pint, P. F. Tortorelli, R. Suzuki, T. Ohdaira, *Appl. Phys. Lett.* **1997**, *71*, 3165.
[50] J. Čížek, O. Melikhova, Z. Barnovská, I. Procházka, R. K. Islamgaliev, *J. Phys. Conf. Ser.* **2013**, *443*, 012008.
[51] L. C. Smedskjaer, M. Manninen, M. J. Fluss, *J. Phys. F Met. Phys.* **1980**, *10*, 2237.
[52] T. Kosub, S. Vélez, J. M. Gomez-Perez, L. E. Hueso, J. Fassbender, F. Casanova, D. Makarov, *Appl. Phys. Lett.* **2018**, *113*, 222409.

© 2022 The Authors. Small published by Wiley-VCH GmbH

16136829, 2022, 17, Downloaded from https://onlinelibrary.wiley.com/doi/10.1002/smll.202201228 by Universitätsbibliothek Basel, Wiley Online Library on [03/09/2024]. See the Terms and Conditions (https://onlinelibrary.wiley.com/terms-and-conditions) on Wiley Online Library for rules of use; OA articles are governed by the applicable Creative Commons License

[53] X. Jia, K. Liu, K. Xia, G. E. W. Bauer, *Europhys. Lett.* **2011**, *96*, 17005.
[54] Y.-T. Chen, S. Takahashi, H. Nakayama, M. Althammer, S. T. B. Goennenwein, E. Saitoh, G. E. W. Bauer, *J. Phys. Condens. Matter.* **2016**, *28*, 103004.
[55] H. Wang, C. Du, P. C. Hammel, F. Yang, *Phys. Rev. B* **2015**, *91*, 220410(R).
[56] A. V. Almaev, B. O. Kushnarev, E. V. Chernikov, V. A. Novikov, P. M. Korusenko, S. N. Nesov, *Superlattices Microstruct.* **2021**, *151*, 106835.
[57] L. Akselrud, Y. u. Grin, *J. Appl. Crystallogr.* **2014**, *47*, 803.
[58] W. Anwand, G. Brauer, M. Butterling, H. R. Kissener, A. Wagner, *Defect Diffus. Forum* **2012**, *331*, 25.
[59] M. O. Liedke, W. Anwand, R. Bali, S. Cornelius, M. Butterling, T. T. Trinh, A. Wagner, S. Salamon, D. Walecki, A. Smekhova, H. Wende, K. Potzger, *J. Appl. Phys.* **2015**, *117*, 163908.
[60] a) A. Van Veen, presented at *4th Int.Workshop on: Slow-Positron Beam Techniques for Solids and Surfaces*, Ontario, Canada, July **1991**; b) J. Dryzek, P. Horodek, *Nucl. Instrum. Methods Phys. Res. B: Beam Interact. Mater. At.* **2008**, *266*, 4000.
[61] P. M. Gordo, L. Liszkay, Z. S. Kajcsos, K. Havancsák, V. A. Skuratov, G. Kögel, P. Sperr, W. Egger, A. P. de Lima, M. F. F. Marques, *Appl. Surf. Sci.* **2008**, *255*, 254.
[62] M. J. Puska, R. M. Nieminen, *Rev. Mod. Phys.* **1994**, *66*, 841.
[63] M. Alatalo, B. Barbiellini, M. Hakala, H. Kauppinen, T. Korhonen, M. J. Puska, K. Saarinen, P. Hautojärvi, R. M. Nieminen, *Phys. Rev. B* **1996**, *54*, 2397.
[64] E. Hirschmann, M. Butterling, U. H. Acosta, M. O. Liedke, A. G. Attallah, P. Petring, M. Görler, R. Krause-Rehberg, A. Wagner, *J. Instrum.* **2021**, *16*, P08001.
[65] V. Olsen, P. Kirkegaard, N. J. Pedersen, M. Eldrup, *Phys. Status Solidi.* **2007**, *4*, 4004.
[66] F. Tuomisto, I. Makkonen, *Rev. Mod. Phys.* **2013**, *85*, 1583.
[67] L. Rondin, J.-P. Tetienne, T. Hingant, J.-F. Roch, P. Maletinsky, V. Jacques, *Rep. Prog. Phys.* **2014**, *77*, 056503.
[68] N. Hedrich, D. Rohner, M. Batzer, P. Maletinsky, B. J. Shields, *Phys. Rev. Applied* **2020**, *14*, 064007.
[69] R. Schoenfeld, W. Harneit, *Phys. Rev. Lett.* **2011**, *106*, 030802.
[70] M. S. Grinolds, S. Hong, P. Maletinsky, L. Luan, M. D. Lukin, R. L. Walsworth, A. Yacoby, *Nat. Phys.* **2013**, *9*, 215.

© 2022 The Authors. Small published by Wiley-VCH GmbH

16136829, 2022, 17, Downloaded from https://onlinelibrary.wiley.com/doi/10.1002/smll.202201228 by Universitätsbibliothek Basel, Wiley Online Library on [03/09/2024]. See the Terms and Conditions (https://onlinelibrary.wiley.com/terms-and-conditions) on Wiley Online Library for rules of use; OA articles are governed by the applicable Creative Commons License